Magnetic Resonance in Medicine 63:1104–1110 (2010)

POCS-Enhanced Correction of Motion Artifacts in Parallel MRI

Alexey A. Samsonov,[1]* Julia Velikina,[2] Youngkyoo Jung,[4] Eugene G. Kholmovski,[5] Chris R. Johnson,[6] and Walter F. Block[1–3]

A new method for correction of MRI motion artifacts induced by corrupted *k*-space data, acquired by multiple receiver coils such as phased arrays, is presented. In our approach, a projections onto convex sets (POCS)-based method for reconstruction of sensitivity encoded MRI data (POCSENSE) is employed to identify corrupted *k*-space samples. After the erroneous data are discarded from the dataset, the artifact-free images are restored from the remaining data using coil sensitivity profiles. The error detection and data restoration are based on informational redundancy of phased-array data and may be applied to full and reduced datasets. An important advantage of the new POCS-based method is that, in addition to multicoil data redundancy, it can use a priori known properties about the imaged object for improved MR image artifact correction. The use of such information was shown to improve significantly *k*-space error detection and image artifact correction. The method was validated on data corrupted by simulated and real motion such as head motion and pulsatile flow. Magn Reson Med 63:1104–1110, 2010. © 2010 Wiley-Liss, Inc.

Key words: POCS; POCSENSE; motion artifact; constrained reconstruction; parallel MRI

Parallel MRI (pMRI) exploits multiple receiver coils to shorten MRI scan times (1–7). In pMRI, acceleration of *k*-space acquisition is achieved by subsampling *k*-space with a reduction factor *R*. Reconstruction of the undersampled data is attainable thanks to n_c-times redundancy of multicoil data, where n_c is the number of receiver coils. Fast data acquisition achievable with pMRI techniques decreases artifacts associated with long MRI scan times; for example, artifacts induced by tissue susceptibility differences and motion effects, such as various physiologic motions and patient movement (8–10). The redundancy of multicoil data can be also exploited for postacquisition correction of many MR image artifacts such as ghosting and flow artifacts in EPI images (11,12) and certain types of motion (13–15).

Typically, motion results in corrupted *k*-space data, which, in turn, causes artifacts in the reconstructed images. It was demonstrated by Bydder et al. (13) that the corrupted samples may be detected comparing pMRI reconstructions of subsets of original dataset. Then, the related artifacts are eliminated by regenerating the identified lines using pMRI methods. The *k*-space errors amenable to such detection and subsequent regeneration should be localized because pMRI techniques may reliably estimate *k*-space samples only on a scale compatible with the spatial frequency bandwidth of the coil sensitivity functions (16). Additionally, the necessity to split the dataset into subsets limits the maximum acceleration factor to $n_c/2$ (13). To avoid limiting requirements that errors be localized in *k*-space, an alternative approach is to correct data using SMASH (SiMultaneous Acquisition of Spatial Harmonics) navigators (14). However, SMASH navigators are only able to handle two-dimensional in-plane translations.

As described before, the pMRI-based motion artifact correction methods rely on data redundancy due to the sensitivity encoding effect and require a priori information about coil sensitivities. Another approach for postacquisition reduction of motion artifacts is to utilize prior information about the imaged object itself to realize the "detect-and-restore" strategy described in the previous paragraph. The projections onto convex sets (POCS) algorithm presents an efficient way to utilize a wide range of such information in image restoration problems (17–19); many POCS-based methods for MRI data artifact correction have been proposed to date (20–24). In our previous work, we adapted the POCS formalism for pMRI data reconstruction (POCSENSE) (7). We showed that utilization of prior information within the POCSENSE framework is an efficient way to reduce noise amplification, thereby affording higher acceleration factors and improving image quality. In this paper, we propose a POCSENSE-based algorithm for the correction of motion artifacts. In our new algorithm, the simultaneous utilization of different sources of information about imaged object (multichannel data and POCS constraints) allows for a significantly more robust *k*-space error detection and artifact correction than can be obtained by applying a pMRI correction alone. If applied with a phase constraint, the new method allows relaxing requirements on the type of *k*-space errors amenable for correction with previously described techniques (13,14). We demonstrate the utility of the new technique on

[1]Department of Radiology, University of Wisconsin, Madison, Wisconsin, USA
[2]Department of Medical Physics, University of Wisconsin, Madison, Wisconsin, USA
[3]Department of Biomedical Engineering, University of Wisconsin, Madison, Wisconsin, USA
[4]Department of Radiology, University of California, San Diego, California, USA
[5]UCAIR, Department of Radiology, University of Utah, Salt Lake City, Utah, USA
[6]Scientific Computing and Imaging Institute, University of Utah, Salt Lake City, Utah, USA

Grant sponsor: NIH NINDS; Grant number: R01NS065034; Grant sponsor: NCI; Grant number: R01CA116380.

*Correspondence to: Alexey A. Samsonov, PhD, Department of Radiology, University of Wisconsin-Madison, WIMR, 1111 Highland Dr., Madison, WI 53705. E-mail: samsonov@wisc.edu

Received 24 July 2009; revised 23 September 2009; accepted 24 September 2009.
DOI 10.1002/mrm.22254
Published online in Wiley InterScience (www.interscience.wiley.com).

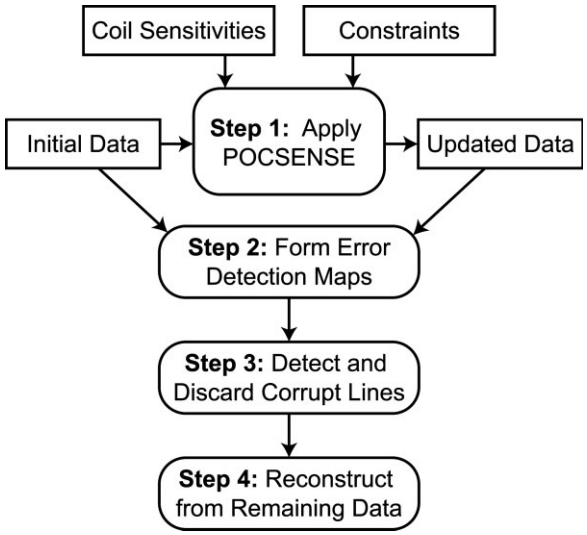

FIG. 1. Block diagram of the proposed motion correction algorithm.

phantom and brain data corrupted by artificial and real motion.

THEORY AND METHODS

POCSENSE (7) exploits the fact that information about image, such as data measurements and most of the commonly used constraints, can be viewed as convex subsets Ω_i ($i = 1,\ldots,n$) of the Hilbert space comprising all possible images (17). The algorithm seeks the solution as a point minimally deviating from all of the available convex sets by employing the projection operators P_i associated with these sets. Therefore, all available data influence the final solution. If the data are consistent, the solution belongs to the (nonempty) intersection of the sets Ω_i. Corruption of data samples creates outliers among otherwise consistent data. Such data samples may drastically bias the solution and cause image artifacts. To reduce the artifacts associated with the erroneous *k*-space samples, the influence of such data on the final image should be minimized (25). We propose to identify the outliers by analyzing distances between the POCSENSE estimate and original data (7). Let $m_i(\boldsymbol{k}), i = 1\ldots n_c$ be initial *k*-space data, and $\tilde{m}_i(\boldsymbol{k})$ be *k*-space estimates after final POCSENSE iteration. The error detection maps are formed as follows:

$$d_i(\boldsymbol{k}) = \tilde{m}_i(\boldsymbol{k}) - m_i(\boldsymbol{k}),\ i = 1, \ldots, n_c \qquad [1]$$

If the initial dataset were consistent, the error maps would be influenced only by noise values. Inconsistent data samples produce significant outliers among the background values. Therefore, identification of inconsistent samples amounts to detection of outlying values in the error maps. To increase the detection power, detection may be performed on one-dimensional detection plots averaged in the readout direction rather than on two-dimensional error maps, because motion usually corrupts an entire *k*-space line in the readout direction. We form the detection plots by summing up n_r absolute values of the error maps in the readout direction and then further improve detection power by adding the results from all coils:

$$p(k_y) = \frac{1}{n_c n_r} \sum_{\gamma=1}^{n_c} \sum_{x} \left| d_\gamma(k_x, k_y) \right| \qquad [2]$$

Samples belonging to the identified corrupted lines are discarded from the dataset, and the image is reconstructed from the remaining data using a pMRI technique. The whole procedure is depicted in Fig. 1. A detailed description of the algorithm steps, including examples of additional constraints, is given in the following sections.

POCS Constraints

As was shown before (13), utilization of pMRI redundancy may identify localized *k*-space errors. In our method, we exploit POCS constraints simultaneously with pMRI to resolve nonlocalized errors (step 1 of the algorithm). One prominent example of a POCS constraint is object support, which has been used extensively in several motion and other artifact correction techniques (20–24). Application of the object support constraint is straightforward and amounts to zeroing out all values outside the prescribed region of support $\boldsymbol{A}$:

$$P_A I(\boldsymbol{r}) = \begin{cases} I(\boldsymbol{r}), & \boldsymbol{r} \in \boldsymbol{A} \\ 0, & otherwise \end{cases} \qquad [3]$$

Another example of POCS constraint is a low-resolution image phase used in reconstruction of partial Fourier (26–28) and pMRI (7,28–30) data. In this paper, we propose to use a low-resolution phase constraint to detect motion-corrupted samples. Image phase can usually be described by a slowly varying function. Ghosting due to motion often introduces a rapidly oscillating frequency component into the image phase, as shown in Fig. 2. Hence, using a low-resolution image phase constraint would bring the image estimate closer to the true image and should improve identification of corrupted *k*-space data. The phase constraint is applied to the input image $I(\boldsymbol{r})$ as follows:

$$P_{\varphi_s} I(\boldsymbol{r}) = M(\boldsymbol{r}) e^{i\varphi_s(\boldsymbol{r})}, \qquad [4]$$

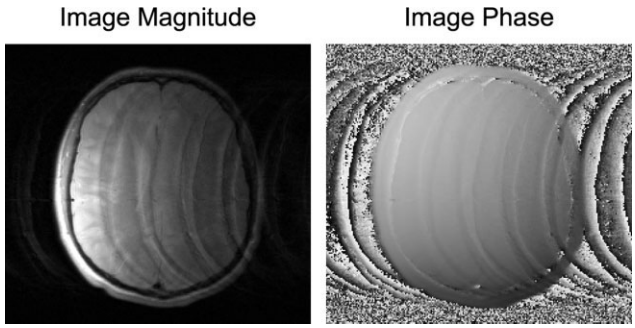

FIG. 2. Magnitude **(a)** and phase **(b)** of an MR image corrupted by motion.

Table 1
Comparison of Error Detection and Correction Methods (POCSENSE and Method of Multiple *k*-Space Copies Regeneration)*

		POCSENSE			
	Multiple *k*-space copies	No constraints	Additional phase constraint	Additional object support	All constraints
Sensitivity	53.5%	76.5%	94.3%	84.4%	96.7%
Specificity	95.6%	96.9%	98.8%	99.7%	99.9%
RMS error	17.4%	11.1%	7.0%	7.6%	6.5%

*Results are averaged among 100 different simulated corruption cases. RMS, root mean square.

where $\varphi_s(\boldsymbol{r})$ is the phase of low-resolution image $I_s(\boldsymbol{r})$ and $M(\boldsymbol{r})$ is the magnitude of the image $I(\boldsymbol{r})$. Since phase constraining exploits the Hermitian symmetry of the Fourier transform of real-valued data, an acceleration mechanism fundamentally different from sensitivity encoding used for pMRI acceleration, we hypothesize that phase constraint may improve error detection. In this study, both object support and phase constraints were applied within the proposed procedure to study the effects of additional knowledge on *k*-space error detection.

Detection of Corrupted Lines and Data Regeneration

As explained above, corrupted data result in the outliers, which we locate by identifying significant peaks in the detection plot generated using Eq. 2. While many methods may be designed to ensure adequate detection of outliers including matching filters and wavelet transforms (31), our experiments demonstrate that a straightforward search for significant local maxima in the plot performs well in identifying peaks. We based our heuristic procedure for peak detection on the signal model used in spectroscopy (32). According to this model, each peak in the raw data can be represented as a sum of the true peak, baseline function, and a constant offset. First, we removed the constant term from the error detection plot by subtracting its minimum value and then normalized it to attain a maximum value of 1. Next, we obtained an approximation of the baseline function by performing soft thresholding of wavelet coefficients calculated for the normalized signal with the universal threshold (33). We used a modification of the widely used Daubechies family of wavelets, the so-called *symlet* wavelets, which are nearly symmetric and also enjoy the desirable properties of orthogonality and compact support (34). We attenuated the signal by the obtained estimate of the baseline. Finally, a point $x(i)$ of the attenuated signal was classified as a peak value if the signal's first difference $\Delta x_i = x_{i+1} - x_i$ satisfied the following three conditions: (1) $\Delta x_i > A$, (2) $\Delta x_{i+k} < -A$ for some $k > 0$, (3) $|\Delta x_{i+j}| < A$ for $0 < j < k$, where the cutoff value A was defined as the mean value of the attenuated signal's difference $|\Delta x|$. This procedure allows for detection of not only localized errors but also corrupted data spanning *k*-space continuously. Therefore, to ensure a fair comparison this procedure was used for error detection in both the proposed method and the method of Bydder et al. (13).

Data

Phantom objects were scanned on a 1.5 T GE Signa scanner (General Electric Healthcare, Waukesha, WI), using a custom-built, four-element ($n_c = 4$), bilateral, temporal lobe, phased-array coil (35). Volunteers were scanned using an eight-channel head (brain data) and neurovascular (neck data) arrays.

Two full datasets of a resolution phantom were collected using a gradient-echo sequence (matrix size 256 × 256, field of view = 14 × 14 cm, pulse repetition time = 100 ms, flip angle = 30°, receiver bandwidth = ±20.83 kHz). The second dataset was obtained after applying a combination of small translational and rotational shifts to the phantom (translation by 0.3 cm, followed by an 8° rotation). Artifacts were induced by substituting the chosen lines of the first dataset with the respective lines of the dataset corresponding to the displaced phantom at randomized positions (a total of 15% of *k*-space lines were corrupted; the center of *k*-space (4% of lines) was not corrupted). One hundred instances of randomly perturbed datasets were created to evaluate the methods' performance (Table 1).

A standard double-echo fast spin echo pulse sequence was used to acquire neck data corrupted by pulsatile motion (echo time = 13.1/85 ms, pulse repetition time = 3 sec, echo train length = 16, receiver bandwidth = 15.63 kHz, slice thickness = 4 mm). A custom double-echo fast spin echo sequence with randomized phase-encoding ordering was used to obtain the brain data corrupted by real motion (echo time = 9/80 ms, pulse repetition time = 5 sec, ETL = 16, receiver bandwidth = 31.25 kHz, slice thickness = 2 mm). A volunteer was asked to intermittently lift and nod his head with random amplitude of 1-3 cm, then return his head to its resting position.

Implementation Details

All data were processed using MATLAB 7 (Mathworks, Natick, MA) environment on a personal computer (Intel Xeon 3.0-GHz processor, 2 GB of random access memory). Nonmodulated sensitivity maps were estimated from reference data, divided by uniform body coil image, and preprocessed using a local polynomial smoothing procedure (1). In vivo coil sensitivities were obtained by apodizing *k*-space data with a Kaiser-Bessel window of radius 32. The estimate of the phase constraint was obtained applying a similar smoothing procedure to the initial image estimate. We used POCSENSE for the final reconstruction of the images. Detection plots for the

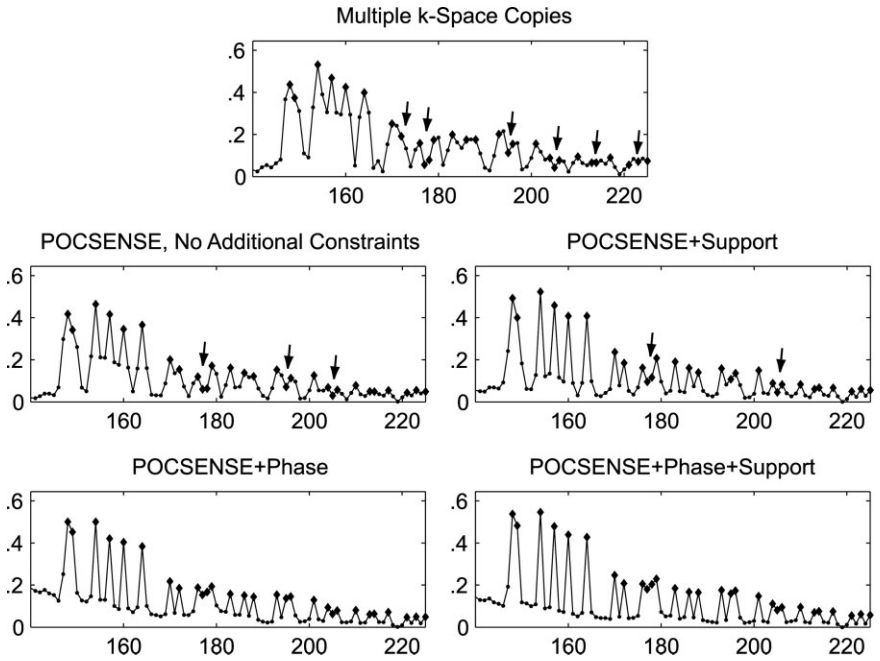

FIG. 3. Comparison of detection plots for different motion-correction approaches (x-axis represents phase-encode direction). Detection plots are formed using method of multiple *k*-space copies regeneration (13) and the proposed method without constraining, with object support, with phase constraint, and both constraints. Arrows point to unresolved *k*-space errors. Inclusion of more information gradually improves identification of corrupted lines. Note excellent resolution of continuous *k*-space errors when detection is attempted with phase constraint.

method of Bydder et al. (13) were formed according to the original description.

We evaluated sensitivity and specificity of error detection and average root mean square error in Monte Carlo experiments on simulated motion corruption of phantom data. The detection sensitivity was defined as the ratio of the number of correctly identified corrupted lines to the total number of corrupted lines. The detection specificity was defined as a ratio of the number of identified uncorrupted lines to the total number of uncorrupted lines. The root mean square error of corrected image was calculated with respect to the ground truth image.

RESULTS

Figure 3 compares detection plots obtained with different methods on artificially corrupted phantom data. One instance from Monte Carlo simulations used to create Table 1 containing both localized and a significant amount of nonlocalized errors is chosen to illustrate error resolution properties of the methods. The plots show that the inclusion of prior information in the form of object support and low-resolution image phase improves the identification of *k*-space error peaks, thereby resulting in an increased sensitivity and specificity of error detection (see Table 1). Using all of the available information provided best detection of corrupted lines. Furthermore, inclusion of a phase constraint allowed a more robust identification of *k*-space errors occupying a contiguous range of phase encodes. These errors were not resolved using coil sensitivity effect alone or in conjunction with object support constraint (black arrows).

Table 1 presents quantitative results of testing the new artifact correction procedure and the method of multiple *k*-space copies (13) on artificially corrupted phantom data in Monte Carlo simulations. As expected from plots in Fig. 3, the new method provides detection of corrupted lines, with higher sensitivity and specificity than of the method of Bydder et al. (13) when nonlocalized errors are present in the data. Inclusion of additional constraints such as object support (Eq. 3), phase smoothness (Eq. 4), or both in the detection procedure further increases the new method's sensitivity and specificity. These increases are accompanied by a significant decrease of root mean square error (from 17.5% for multiple *k*-space copies down to 6.4% for POCSENSE with all constraints).

Table 2 shows results of simulations with different numbers of intact central *k*-space lines. As may be expected, the performance of phase constraint decreases with the width of uncorrupted *k*-space center. However, even for the small number of total uncorrupted lines in the *k*-space center (around 2% of the total number of lines), significant improvement over the other methods was observed. In extreme cases of corruption (0%, the central *k*-space line is corrupted),

Table 2
Comparison of Error Detection of POCSENSE With Phase Constraint for Different Sizes of Uncorrupted *k*-Space Center for Self-Calibrated Phase Estimation Approach

Uncorrupted center lines (%)	0	0.8	1.6	2.4	3.2	4
Sensitivity	68.2%	76.0%	86.9%	92.1%	92.1%	94.3%
Specificity	92.3%	93.9%	96.9%	97.9%	99.3%	98.8%
RMS error	24.58%	15.2%	11.3%	8.1%	7.4%	7%

RMS, root mean square.

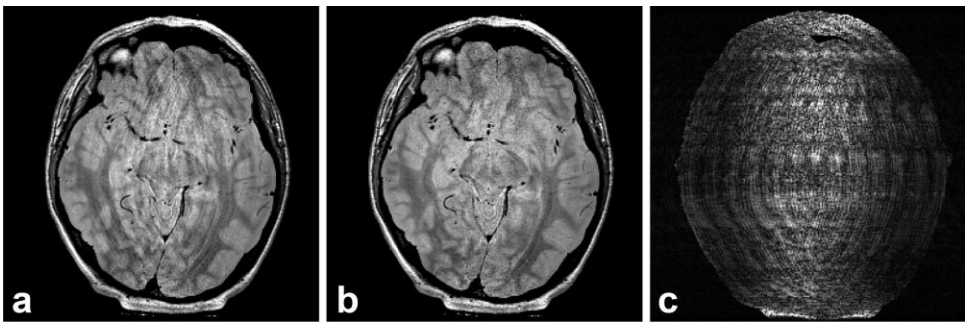

FIG. 4. Correction of brain data corrupted by bulk motion. **a:** Corrupted image. **b:** Corrected image. **c:** Absolute value of difference between **(a)** and **(b)** (×4).

phase constraint resulted in the lowest sensitivity and specificity.

Figure 4 shows results of correcting brain data corrupted by intentional motion acquired with a randomized phase-encoding scheme. The true coil sensitivities were used in the correction procedure. Even though randomization of phase encodes leads to less coherent ghosts than in the case of regular sampling, significant artifacts still arise in the image. The proposed technique eliminates even subtle ghosting arising from the corruption of high spatial frequencies.

Figure 5 shows results of correction of neck images corrupted by pulsatile flow of cerebrospinal fluid (CSF). The signal intensity of the CSF around spinal cord is distributed among ghosts in the phase-encode direction due to motion (Fig. 5a). The in vivo coil sensitivities were used for artifact correction. Both unconstrained (to lesser degree) and constrained (to higher degree) POCSENSE correction decreased ghosting in the reconstructed images, as can be seen in Fig. 5b,c. These improvements are further illustrated by the differences between the corrupted and corrected images displayed in Fig. 5g,h, with a scaling factor of 4. The magnified images clearly demonstrate decreased and heterogeneous signal in CSF ring around spinal cord due to motion-induced ghosting (Fig. 5d). Simultaneously with ghost artifact minimization, POCSENSE-based correction restored intensity and improved homogeneity of the region (Fig. 5e). We detected most improvement when POCSENSE-based error detection is applied simultaneously with object support and phase constraints (Fig. 5f).

DISCUSSION AND CONCLUSIONS

We developed a new method for correction of MRI artifacts induced by corrupted multicoil *k*-space data. The new method relies on informational redundancy of phased-array data acquisition and POCS constraints for a robust error detection and artifact correction. Compared to the method proposed in Bydder et al. (13), the new method is much more sensitive and specific in error detection and more efficient in artifact suppression (Table 1). While sensitivity and specificity of error detection are also tightly connected with the choice of a peak detection procedure, detection plots in Fig. 3 clearly illustrate the basis for demonstratively improved error detection. The new method also allows for correction of data sampled with reduction factors above the previously realized limit of $n_c/2$ (13).

In practice, the maximum reduction factor for data amenable to correction by the proposed technique depends on the total number of corrupted lines. In general, data left after discarding the erroneous samples should possess enough information redundancy for image reconstruction; that is, the final reduction factor should not exceed the number of coils. If discarding erroneous data leads to large gaps of missing data (more than amenable to reconstruction with a given number of coil receivers), pMRI interpolation of such gaps may lead to a badly conditioned problem. The accompanying SNR decrease in the corrected images will be due to two factors: reduction of data lines and g-factor noise amplification (1). While SNR degradation due to the first factor is straightforward to calculate, the g-factor degradation will depend on many factors, most important of which is the size of contiguous gaps of data corrupted by motion. Obviously, motion corrupting large contiguous *k*-space areas is not amenable to correction with the proposed technique. In case of such a severe corruption, a repeated scan may still be necessary.

The sensitivity of motion correction will depend on the peak-to-noise values in the detection plot. Height of the peaks in the error detection plots depends both on the severity of motion and on the energy of *k*-space data in the corrupted regions. Since energy in *k*-space for realistic objects falls off rapidly toward *k*-space edges, one may expect that detection of samples in *k*-space areas of higher spatial frequencies may be jeopardized in low SNR acquisitions. For most non-Cartesian trajectories, however, this issue may become less problematic, as detection plots may be built summing up data points along the radial direction (for radials) or along individual interleaves (for spirals). In this case, because the *k*-space center is sampled for every readout, contributions from the corrupted *k*-space center will facilitate identification of the corrupted readout.

An important characteristic of the new algorithm is that it can easily adapt to include a priori information about the imaged object that may be represented as POCS constraints. Such information may be complementary to the data redundancy due the sensitivity encoding, and, hence, may improve artifact correction. We demonstrated that utilization of such constraints simultaneously with sensitivity encoding improves *k*-space error detection and even relaxes a requirement on locality of *k*-space inconsistencies, which is necessary when pMRI

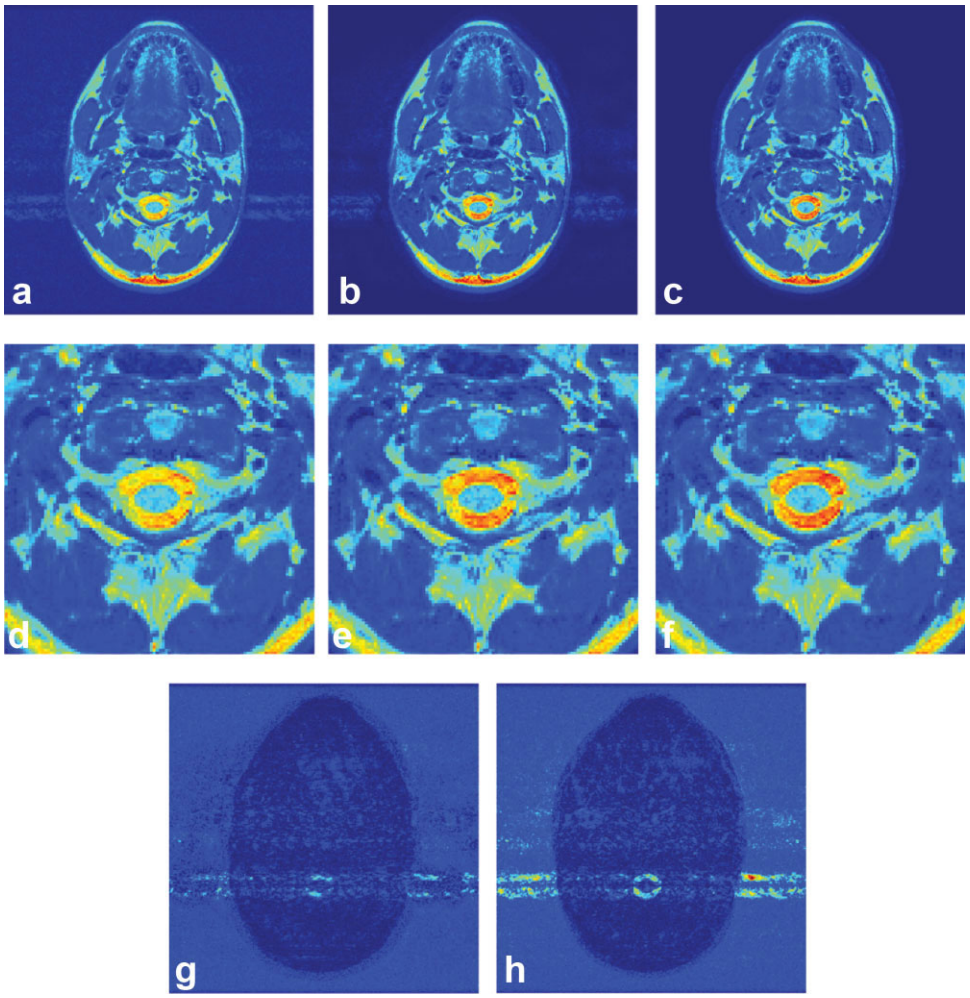

FIG. 5. Correction of neck images corrupted by pulsatile motion of CSF. Corrupted image **(a)** was corrected by the proposed method both without **(b)** and with support and phase constraints **(c)**. The corresponding magnified images are given in **(d,e,f)**, respectively. Note the increase in CSF intensity and its homogeneity around spinal cord from **(d)** to **(e)** to **(f)**. The mean values within the CSF ring are 0.901, 0.986, and 1.019 for uncorrected **(d)**, POCSENSE-corrected **(e)**, and POCSENSE+support+phase-corrected **(f)** cases, respectively. The differences between corrupted and corrected images **(b,c)** (×4) illustrating the removed artifacts are given in **(g)** and **(h)**, respectively.

artifact correction procedure is applied on its own. In particular, we demonstrated that using object support, phase smoothness constraints, or both significantly improves sensitivity and specificity of error detection. While object support constraint has been previously used (22), application of smooth phase constraint for motion correction, to the best of our knowledge, is novel. As the phase constraint utilizes data redundancy due to Hermitian symmetry of Fourier transform, the requirement on localization of *k*-space errors imposed by sensitivity encoding becomes less stringent (Fig. 3). Tables 1 and 2 also show that smooth phase constraint outperforms the object support constraint in the case when an adequate phase estimate may be obtained from low-resolution images. Therefore, using the phase smoothness constraint (Eq. 4) may be important for motion artifact correction when object support constraint is of limited extent and/or when it is desirable to avoid the associated postprocessing. Provisions should be made to ensure that an adequate estimate of phase is available. To ensure that the *k*-space center is not corrupted, several possible ways may be suggested. First, obtaining phase estimate may be a part of a reference scan used to calibrate pMRI (36). Second, a synergetic combination of the multiple *k*-space copies method of Bydder et al. (13) and the proposed method may be used. In this approach, detection of corrupted samples and restoration of image are interleaved with estimation of coil sensitivities and image phase, leading to refinement of coil sensitivities and image phase estimate. As the method of Bydder et al. (13) works best at the *k*-space center, it may be used in the first place to correct *k*-space center and obtain error-free coil sensitivity estimates. Then, the proposed method with refined image phase may be used to resolve the rest of *k*-space errors.

A conceptually related approach was recently proposed for three-dimensional radial diffusion-weighted imaging in steady state (37). In this approach, radial lines corrupted during application of diffusion gradients were determined by detecting outliers in distribution of the centers of mass of radial lines and restored using pMRI reconstruction. The utility of the POCSENSE-based method for correction of motion artifacts in diffusion-weighted acquisitions is currently under investigation.

While our method does not rely on specific models of object motion, it achieves best correction when most data form a consistent subset or the object spends a large amount of time in a "baseline" position. The method was applied to correct patient head motion (Fig. 4) and pulsatile motion (Fig. 5). Another potential application is cardiac cine imaging with prospective cardiac gating in patients with arrhythmia, where motion artifacts may

be introduced because of degraded correlation between ECG events and cardiac motion. As we have demonstrated, utilization of additional constraints may improve detection of nonlocalized *k*-space errors (Fig. 3; Table 1). However, the corresponding gaps in *k*-space data should be narrow enough to allow restoration with the given number of receiver coils. Hence, the motion correction procedure will still benefit from localization of *k*-space errors. Such localization can be promoted using sequences with randomized phase encodings, when corruption due to continuous motion becomes randomly distributed from line to line in *k*-space. Additionally, the maximum width of contiguous gaps of eliminated data may be artificially restricted to reduction factors feasible with a given coil array.

Practical implementation of the proposed method may vary, depending on application. In segmented scans such as fast spin echo sequences, the motion may be expected to corrupt the whole echo train. Hence, more benefits are expected when the whole echo train is eliminated. In fast gradient echo-based sequences, not only detected corrupted readouts but also readouts acquired in immediate time intervals may be eliminated to ensure robust correction. In case of calibration in a separate calibration scan, extrapolation of coil sensitivity maps outside object support seen in the reference scan toward field of view edges is an adequate choice to ensure that final coil sensitivity maps cover the area of possible object positions during the scan (1). Finally, the new method is expected to handle artifacts caused by *k*-space spike noise (38).

REFERENCES

1. Pruessmann KP, Weiger M, Scheidegger MB, Boesiger P. SENSE: sensitivity encoding for fast MRI. Magn Reson Med 1999;42:952–962.
2. Sodickson DK, Manning WJ. Simultaneous acquisition of spatial harmonics (SMASH): ultra-fast imaging with radiofrequency coil arrays. Magn Reson Med 1997;38:591–603.
3. Bydder M, Larkman DJ, Hajnal JV. Generalized SMASH imaging. Magn Reson Med 2002;47:160–170.
4. Kyriakos WE, Panych LP, Kacher DF, Westin CF, Bao SM, Mulkern RV, Jolesz FA. Sensitivity profiles from an array of coils for encoding and reconstruction in parallel (SPACE RIP). Magn Reson Med 2000; 44:301–308.
5. Griswold MA, Jakob PM, Heidemann RM, Nittka M, Jellus V, Wang J, Kiefer B, Haase A. Generalized autocalibrating partially parallel acquisition (GRAPPA). Magn Reson Med 2002;47:1202–1210.
6. Sodickson DK, McKenzie CA. A generalized approach to parallel magnetic resonance imaging. Med Phys 2001;28:1629–1643.
7. Samsonov AA, Kholmovski EG, Parker DL, Johnson CR. POCSENSE: POCS-based reconstruction for sensitivity encoded MRI. Magn Reson Med 2004;52:1397–1406.
8. Weiger M, Pruessmann KP, Österbauer R, Börnert P, Boesiger P, Jezzard P. Sensitivity-encoded single-shot spiral imaging for reduced susceptibility artifacts in BOLD fMRI. Magn Reson Med 2002;48: 860–866.
9. Bammer R, Keeling SL, Augustin M, Pruessmann KP, Wolf R, Stollberger R, Hartung HP, Fazekas F. Improved diffusion-weighted single-shot echo-planar imaging (EPI) in stroke using sensitivity encoding (SENSE). Magn Reson Med 2001;46:548–554.
10. Weiger M, Pruessmann KP, Boesiger P. Cardiac real-time imaging using SENSE. Magn Reson Med 2000;43:177–184.
11. Kuhara S, Kassai Y, Ishihara Y, Yui M, Hamamura Y, Sugimoto H. A novel EPI reconstruction technique using multiple RF coil sensitivity maps. In: Proceedings of the 8th Annual Meeting of ISMRM, Denver, 2000. p 154.
12. Kellman P, McVeigh E. Ghost artifact cancellation using phased array processing. Magn Reson Med 2001;46:335–343.
13. Bydder M, Larkman DJ, Hajnal JV. Detection and elimination of motion artifacts by regeneration of *k*-space. Magn Reson Med 2002; 47:677–686.
14. Bydder M, Atkinson D, Larkman DJ, Hill DLG, Hajnal JV. SMASH navigators. Magn Reson Med 2003;49:493–500.
15. Atkinson D, Larkman DJ, Batchelor PG, Hill DL, Hajnal JV. Coil-based artifact reduction. Magn Reson Med 2004;52:825–830.
16. Wang Y. Description of parallel imaging in MRI using multiple coils. Magn Reson Med 2000;44:495–499.
17. Youla DC, Webb H. Image restoration by the method of convex projections: part 1—theory. IEEE Trans Med Imaging 1982;1:81–94.
18. Haacke EM, Liang ZP, Boada F. Constrained reconstruction using projection onto convex sets and model constraints and for the removal of phase, motion and Gibbs artifacts in magnetic resonance imaging and ultrasound imaging. Optic Eng 1990;29:555–566.
19. Liang ZP, Boada FE, Constable RT, Haacke EM, Lauterbur PC, Smith MR. Constrained reconstruction methods in MR imaging. Rev Magn Reson Med 1992;4:67–185.
20. Hedley M, Yan H, Rosenfeld D. Motion artifact correction in MRI using generalized projections. IEEE Trans Med Imaging 1991;10: 40–46.
21. Riek JK, Tekalp AM, Smith WE, Kwok E. Out-of-plane motion compensation in multislice spin echo MRI. IEEE Trans Med Imaging 1995;14:464–470.
22. Weerasinghe C, Yan H. An improved algorithm for rotational motion artifact suppression in MRI. IEEE Trans Med Imaging 1998;17: 310–317.
23. Kholmovski EG, Samsonov AA, Parker DL. Motion artifact reduction technique for dual-contrast FSE imaging. Magn Reson Imaging 2002; 20:455–462.
24. Lee KJ, Barber DC, Paley MN, Wilkinson ID, Papadakis NG, Griffiths PD. Image-based EPI ghost correction using an algorithm based on projection onto convex sets (POCS). Magn Reson Med 2002;47: 812–817.
25. Bydder M. The use of robust methods to reduce image artifacts. In: Proceedings of the 11th Annual Meeting of ISMRM, Toronto, 2003. p 482.
26. Noll DC, Nishimura DG, Macovski A. Homodyne detection in magnetic resonance imaging. IEEE Trans Med Imaging 1991;10:154–163.
27. Haacke EM, Lindskog ED, Lin W. A fast, iterative, partial-Fourier technique capable of local phase recovery. J Magn Reson Imaging 1991;92:126–145.
28. Bydder M, Robson MD. Partial Fourier partially parallel imaging. Magn Reson Med 2005;53:1393–1401.
29. Willig-Onwuachi JD, Yeh EN, Grant AK, Ohliger MA, McKenzie CA, Sodickson DK. Phase-constrained parallel MR image reconstruction. J Magn Reson 2005;176:187–198.
30. Lew C, Pineda AR, Clayton D, Spielman D, Chan F, Bammer R. SENSE phase-constrained magnitude reconstruction with iterative phase refinement. Magn Reson Med 2007;58:910–921.
31. Unser M, Aldroubi A. A review of wavelets in biomedical applications. Proc IEEE 1996;84:626–638.
32. Du P, Kibbe WA, Lin SM. Improved peak detection in mass spectrum by incorporating continuous wavelet transform-based pattern matching. Bioinformatics 2006;22:2059–2065.
33. Donoho D, Johnstone I. Ideal spatial adaptation by wavelet shrinkage. Biometrika 1993;81:425–455.
34. Mallat S. A theory of multi-resolution signal decomposition: the wavelet representation. IEEE Trans Pattern Anal Mach Intell 1989;11: 674–693.
35. Hadley JR, Chapman BE, Roberts JA, Chapman DC, Goodrich KC, Buswell HR, Alexander AL, Tsuruda JS, Parker DL. A three-coil comparison for MR angiography. J Magn Reson Imaging 2000;11:458–468.
36. Willig-Onwuachi J, Yeh EN, Grant AK, Ohlinger MA, McKenzie CA, Sodickson DK. Phase-constrained parallel MR image reconstruction. J Magn Reson 2005;176:187–198.
37. Jung YK, Samsonov AA, Block WF, Lazar M, Lu A, Jing Liu, Alexander AL. 3D diffusion tensor MRI with isotropic resolution using a steady-state radial acquisition. J Magn Reson Imaging 2009; 29:1175–1184.
38. Kao YH, MacFall JR. Correction of MR *k*-space data corrupted by spike noise. IEEE Trans Med Imaging 2000;19:671–680.